

# Hybrid Electrolytes Enabling in-situ Interphase Protection and Suppressed Electrode Dissolution for Aqueous Sodium-Ion Batteries

Hao Wang<sup>+, [a, b]</sup> Tingting Liu<sup>+, [a, c]</sup> Xiaofan Du<sup>+, [a, d]</sup> Jinzhi Wang,<sup>[a, c]</sup> Yuanyuan Yang,<sup>[a, c]</sup> Huayu Qiu,<sup>[a]</sup> Guoli Lu,<sup>[c, e]</sup> Hongliang Li,<sup>[b]</sup> Zheng Chen,\*<sup>[a, d]</sup> Jingwen Zhao,\*<sup>[a, d]</sup> and Guanglei Cui\*<sup>[a, e]</sup>

Aqueous sodium-ion batteries are promising candidates for grid-scale energy storage due to their high safety and low cost. However, the constant dissolution of vanadium-based electrodes and protective solid-electrolyte interphase (SEI) in aqueous electrolytes severely limits the cycle life. Herein, using adiponitrile as a functional co-solvent, we designed a super-concentrated aqueous sodium electrolyte ( $\text{Na}^+/\text{H}_2\text{O}=1$ , molar ratio) to confine almost all water molecules within the primary solvation shell of  $\text{Na}^+$  with decreased activity. Such a unique solvation

structure not only expands the electrochemical stability window of the electrolyte to 2.75 V, but also greatly alleviates the dissolution of vanadium-based electrodes and NaF-rich SEI. The assembled  $\text{Na}_3\text{V}_2(\text{PO}_4)_3/\text{NaTi}_2(\text{PO}_4)_3$  battery delivers an average Coulombic efficiency of 99.6% with 71% capacity retention after 1000 cycles at 5 C. In addition, the freezing point of the electrolyte could be reduced  $-79^\circ\text{C}$  while retaining appreciable low-temperature conductivity due to the disrupted hydrogen bond among water molecules.

## Introduction

Although lithium-ion batteries (LIBs) are already widely used in portable electronics and electric vehicles, the resource availability issue of lithium along with potential safety hazard brought by flammable organic electrolytes will be a great obstacle in the emerging grid-scale energy storage applications.<sup>[1]</sup> Contrary to lithium, sodium (Na) is highly abundant in both ocean and earth crust. Sodium-ion batteries

(SIBs) that operate in aqueous electrolytes hold great promise in large-scale energy storage where cost, safety and cycle-life outweigh energy density considerations.<sup>[2]</sup> Unfortunately, conventional aqueous electrolytes undergo severe parasite hydrogen evolution reaction (HER) and oxygen evolution reaction (OER) due to the narrow electrochemical stability windows (ESWs) of water ( $\sim 1.23$  V).<sup>[3]</sup> Moreover, the widely used vanadium-based cathodes in sodium-ion batteries suffer from constant vanadium dissolution in aqueous electrolytes,<sup>[4]</sup> further deteriorating the cycling performance of aqueous SIBs.

Inspired by the “water-in-salt electrolyte” (WiSE) concept, Wang et al. developed a highly concentrated 9 mol/L (m) sodium trifluoromethane sulfonate (NaOTf) aqueous electrolyte which could generate a protective anion-derived NaF-rich solid-electrolyte interphase (SEI) on the anode surface and kinetically inhibit HER to some extent.<sup>[5]</sup> However, this highly concentrated NaOTf electrolyte still contains non-negligible amounts of water ( $\text{Na}^+/\text{H}_2\text{O}=6$ , molar ratio), which not only causes the partial dissolution of NaF-rich SEI component, but also hardly eliminates the electrode dissolution issue, especially at low cycling rates. Efforts aiming to further increase the salt concentration achieved limited success, due to the much lower solubility of typical sodium salts with fluorinated anions ( $\sim 9$  m) than their Li counterparts ( $\sim 22$  m).<sup>[6]</sup> In addition, those saturated electrolyte solutions generally have relatively high freezing points due to the prevalence of hydrogen bonding networks among water molecules, which severely limits the low-temperature applications of aqueous SIBs.<sup>[7]</sup>

Alternatively, hybrid aqueous electrolytes coupled with nonaqueous co-solvents offer technical superiority over typical concentrated aqueous electrolytes in terms of the possible combinations of merits from both aqueous (fast ion transport,

[a] H. Wang,<sup>+</sup> T. Liu,<sup>+</sup> Dr. X. Du,<sup>+</sup> J. Wang, Y. Yang, H. Qiu, Dr. Z. Chen, Dr. J. Zhao, Prof. G. Cui  
Qingdao Institute of Bioenergy and Bioprocess Technology  
Chinese Academy of Sciences  
Qingdao 266101, P.R. China  
E-mail: chenzheng@qibebt.ac.cn  
zhaojw@qibebt.ac.cn  
cuigl@qibebt.ac.cn

[b] H. Wang,<sup>+</sup> H. Li  
Institute of Materials for Energy and Environment  
Qingdao University  
Qingdao 266071, P.R. China

[c] T. Liu,<sup>+</sup> J. Wang, Y. Yang, G. Lu  
University of Chinese Academy of Sciences  
Beijing 100049, P.R. China

[d] Dr. X. Du,<sup>+</sup> Dr. Z. Chen, Dr. J. Zhao  
Shandong Energy Institute  
Qingdao, 266101, China

[e] G. Lu, Prof. G. Cui  
School of Future Technology  
University of Chinese Academy of Sciences  
Beijing 100049, P.R. China

[+] These authors contributed equally to this work.

 Supporting information for this article is available on the WWW under  
<https://doi.org/10.1002/batt.202200246>

 An invited contribution to a Special Collection dedicated to Aqueous Electrolyte Batteries

high safety) and nonaqueous (high chemical and electrochemical stability, limited SEI and electrode dissolution) systems.<sup>[8]</sup> Besides, the presence of nonaqueous solvents could promote the breaking of hydrogen bonding interactions between water molecules and thus widen the available temperature range for stable solutions. For example, Wang et al. introduced dimethyl carbonate into WiSE to expand the electrochemical window of an aqueous lithium electrolyte to 4.1 V.<sup>[8a]</sup> Similarly, Dou et al. proposed an “acetonitrile/water-in-salt” concept in lithium electrolyte, which could offer a wide ESW up to ~3.0 V (on stainless steel electrodes).<sup>[8b]</sup> Very recently, Liu et al. reported a hybrid aqueous electrolyte with a freezing point lower than -110°C by adding sulfolane as a co-solvent to an aqueous solution of LiClO<sub>4</sub>.<sup>[9]</sup> However, the beneficial role of organic co-solvents remains less explored in SIBs.<sup>[10]</sup> More importantly, compared with the LiF-rich SEI reported in aqueous lithium-ion batteries, NaF-rich SEI formed in aqueous sodium electrolyte is much less stable due to the much higher solubility of NaF (>40 mg mL<sup>-1</sup> at 25°C) than LiF (<1.34 mg mL<sup>-1</sup> at 25°C) in water.<sup>[6]</sup> As a result, forming a robust NaF-rich SEI remains a challenge in the aqueous phase. Apparently, the criteria for ideal co-solvents are stringent as practically feasible aqueous sodium electrolytes should simultaneously meet several key requirements, such as high tolerance toward electrochemical decomposition, minimal dissolution of SEI and electrodes as well as low-temperature adaptability.

In this work, we use adiponitrile (ADN), a high-voltage additive commonly used for lithium-ion batteries, as a co-solvent to design a hybrid super-concentrated aqueous sodium electrolyte with an ultra-high Na<sup>+</sup>/H<sub>2</sub>O molar ratio of 1:1. The introduced ADN disrupts the hydrogen bonding network among water molecules and reduces the freezing point of the electrolyte to -79°C while retaining appreciable low-temperature conductivity. More importantly, almost all water molecules are confined in the primary solvation shell of Na<sup>+</sup> with decreased activity. This unique solvation structure not only delays OER and extends the ESW to 2.75 V, but also minimizes dissolution chances of NaF-rich SEI and vanadium-based electrodes. Consequently, the assembled Na<sub>3</sub>V<sub>2</sub>(PO<sub>4</sub>)<sub>3</sub>/NaTi<sub>2</sub>(PO<sub>4</sub>)<sub>3</sub> full cell delivers an average Coulombic efficiency (CE) of 99.6% with 71% capacity retention after 1000 cycles at 5 C.

## Results and Discussion

To achieve long cycle life of SIBs with a wide operation temperature range based on hybrid aqueous electrolytes, it is essential to select a suitable co-solvent, considering an expected balance between satisfactory ESWs and suppressed dissolution of SEI and vanadium-based electrodes, and favorable low temperature performance at the same time. ADN is commonly used as a high-voltage additive in LIBs due to its extremely high oxidation stability.<sup>[11]</sup> Moreover, ADN has a donor number of ~14, which is much lower than that of water (~18).<sup>[12]</sup> Thus, Na<sup>+</sup> is likely to be preferentially coordinated by water instead of ADN in the hybrid electrolyte. As a result,

decreased amounts of free water can be anticipated in hybrid electrolytes, which could effectively suppress the dissolution issues that afflict aqueous SIBs. Besides, it is known that dinitrile molecules featuring cyano group serve as hydrogen bond acceptors, which could theoretically facilitate the disruption of hydrogen bond network among water molecules and thus reduce the freezing point of aqueous electrolytes.<sup>[13]</sup> All these features make ADN an ideal co-solvent for the aqueous sodium electrolytes.

The hybrid aqueous sodium electrolytes were prepared by dissolving NaTFSI salt into ADN/H<sub>2</sub>O mixed solvents and the as-prepared samples are named as 1Na-1H<sub>2</sub>O-xADN for short with the molar ratio of 1:1:x (x=1, 1.8, 2.5, 3.5, 5). A clear and colorless hybrid electrolyte solution (Figure S1) can be obtained with a NaTFSI:H<sub>2</sub>O:ADN molar ratio of 1:1:2.5 (abbreviated as AWE). It possesses the highest ionic conductivity of 3.39 mS cm<sup>-1</sup> at room temperature among different molar ratios of H<sub>2</sub>O:ADN (Figure 1a) and therefore is chosen in the following electrochemical and spectroscopic tests.<sup>[14]</sup> A SIB comprising Na<sub>3</sub>V<sub>2</sub>(PO<sub>4</sub>)<sub>3</sub> (NVP) cathode and NaTi<sub>2</sub>(PO<sub>4</sub>)<sub>3</sub> (NTP) anode (XRD data of NVP and NTP shown in Figure S2) based on AWE shows satisfied rate performance due to its moderately high conductivity (Figure S3). Differential scanning calorimetry (DSC) curve of the AWE electrolyte displays a freezing point of -79°C (Figure 1b), significantly lower than the routine salt-concentrated 9 m NaTFSI electrolyte (-16°C). This vast disparity in the liquidus temperature range rationalizes the role of ADN in inducing eutectic interactions among electrolyte components.<sup>[15]</sup>

It is well known that the freezing point of aqueous electrolytes is heavily influenced by the inter-molecular hydrogen bonding interaction.<sup>[16]</sup> Hence, the hydrogen bonding structures of AWE and 9 m NaTFSI electrolytes are investigated with pure water as a comparison. FTIR spectra of pure water in Figure 1c displays a broad band between 3100 and 3650 cm<sup>-1</sup>, which is ascribed to OH stretching vibration of water in various hydrogen bonding environments. For the highly concentrated 9 m NaTFSI (Na<sup>+</sup>/H<sub>2</sub>O=6, molar ratio), the peak at ~3600 cm<sup>-1</sup> corresponding to coordinated water increases while the peak at ~3380 cm<sup>-1</sup> corresponding to free water (also called liquid water) is greatly reduced.<sup>[17]</sup> However, the band associated with free water still exists, revealing the presence of hydrogen bonding between free water molecules in 9 m NaTFSI. For the super-concentrated AWE (Na<sup>+</sup>/H<sub>2</sub>O=1, molar ratio), the signal of hydrogen bonding between free water molecules vanished, which contributes to the low freezing point of AWE electrolyte. As a result, the AWE electrolyte exhibits a moderate ionic conductivity of 1.19 mS cm<sup>-1</sup> even at -20°C (Figure 1d), which indicates sufficient ion transport at low-temperature. In addition, we also noted that the peak associated to coordinated water almost disappeared in the AWE, which further signifies the extremely low content of water in the super-concentrated AWE. A SIB based on NVP cathode and NTP anode was assembled to evaluate the low temperature performance of the AWE electrolyte ranging from 0°C to -20°C. As the temperature decreases from 0°C to -20°C, 94.8% of the original capacity still maintained (Figure 1e),

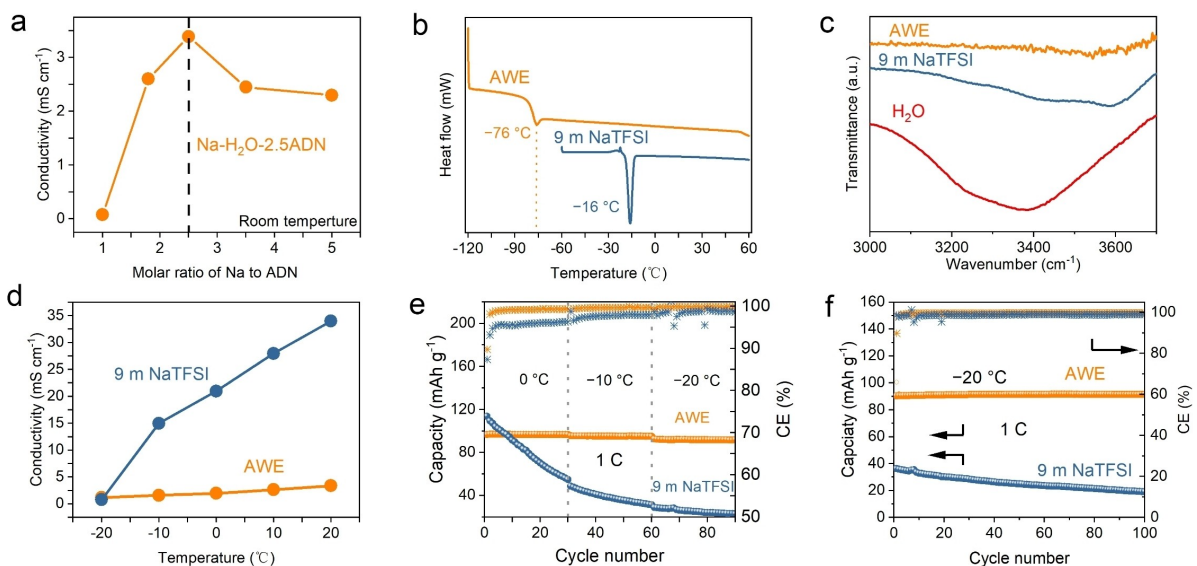


**Figure 1.** a) Ionic conductivity of NaTFSI-H<sub>2</sub>O-ADN electrolytes with different NaTFSI :H<sub>2</sub>O:ADN molar ratios (1:1:1, 1:1:1.8, 1:1:2.5, 1:1:3.5, 1:1:5) at room temperature. b) DSC curves of AWE and 9 m NaTFSI electrolytes. c) FTIR spectra of AWE and 9 m NaTFSI electrolytes with pure water as a comparison. d) Ionic conductivity of the AWE at different temperatures. e) Discharge capacity of NVP/NTP using AWE in low-temperature region. f) Cycling stability and Coulombic efficiency of NVP/NTP full cell operated in AWE and 9 m NaTFSI electrolytes at 1 C under -20 °C.

which demonstrated the superior low temperature performance of the AWE electrolyte. Moreover, no capacity fading of the SIB based on the AWE electrolyte is observed at a low temperature of -20 °C after 100 cycles (Figure 1f). As a comparison, the capacity of SIB adopting the routine salt-concentrated electrolyte (9 m NaTFSI) decreases by 63% in merely 20 cycles.

Since the long cycle life of aqueous SIBs requires an electrolyte with a wide electrochemical stability window, especially high reduction stability to alleviate HER, the reduction stability of the AWE electrolyte was first investigated. The onset potential of HER in AWE and 9 m NaTFSI electrolytes were evaluated by linear sweep voltammetry (LSV) at a scan rate of 0.5 mV s<sup>-1</sup> on Pt electrodes because of the strong catalytic effect of Pt toward HER which represents a harsher environment. Figure 2a shows that the onset potential of HER in 9 m NaTFSI and AWE locates at -0.88 V and -1.21 V (vs. Ag/AgCl) respectively. LSV tests were also performed using Al foil as the working electrodes, and the superior reduction stability of AWE was still remarkable (Figure S4). A more aggressive floating test at a fixed potential of -1.2 V vs. Ag/AgCl was also carried out to compare the cathodic stability of electrolytes. A large cathodic current up to 0.5 mA cm<sup>-2</sup> can be observed in the 9 m NaTFSI electrolyte accompanied with obvious bubble generation on Pt electrode surface during the floating test (Figures 2b and S5), which indicates significant parasite HER of the 9 m NaTFSI electrolyte at low potential. Under the identical condition, the AWE electrolyte displays an order of magnitude lower cathodic current with no visible bubble on the Pt electrode surface, which demonstrates its much higher reduction stability.

The high reduction stability of AWE due to the suppressed HER can be also illustrated in the electrochemical performance

of NTP/AC (AC refers to activated carbon) half-cell, as the cell supported by AWE shows much higher CE with superior cycling performance compared with the one based on 9 m NaTFSI electrolyte (Figures S6 and S7). Online electrochemical mass spectrometry (OEMS) (Figure S8) enabling quantitative study of evolved H<sub>2</sub> was further employed to compare the amount of produced H<sub>2</sub> using AWE and 9 m NaTFSI electrolytes in NVP/NTP cell under the working conditions. A large amount of H<sub>2</sub> was observed at high state-of-charge (SOC) during charge/discharge of NVP/NTP cell in 9 m NaTFSI (Figure 2c), indicating severe water reductive decomposition reaction. Gratifying, the H<sub>2</sub> signal was below the detection limit for the cell adopting the AWE (Figure 2d), which proved the substantially alleviated HER in AWE.

It is widely recognized that HER in aqueous batteries can be kinetically suppressed by SEI generated from the decomposition of F-containing anions.<sup>[18]</sup> Compared with the LiF-rich SEI reported in aqueous lithium-ion battery, NaF-rich SEI formed in aqueous sodium electrolyte is much less stable due to the much higher solubility of NaF (>40 mg mL<sup>-1</sup> at 25 °C) than LiF (<1.34 mg mL<sup>-1</sup> at 25 °C) in water.<sup>[5b]</sup> Therefore, for aqueous SIBs, constructing a robust SEI with minimal dissolution is critical for suppressed HER. To gain insights into the inhibited HER using the AWE electrolyte, the composition and morphology of SEI on NTP anode after cycling was explored. Figure 3(a) shows results of surface analysis by X-ray photoelectron spectroscopy (XPS) of the NTP electrode after 50 cycles in AWE. The F1s signal can be deconvoluted into contributions from the binder polyvinylidene fluoride (PVDF) (689.2 eV) used in the electrode, certain -CF<sub>3</sub> species generated by the decomposition of salt anion TFSI<sup>-</sup> (688.8 eV), and inorganic fluoride NaF (684.8 eV) which is usually regarded as the useful component in SEI.<sup>[19]</sup> It is apparent that the intensity of the protective NaF

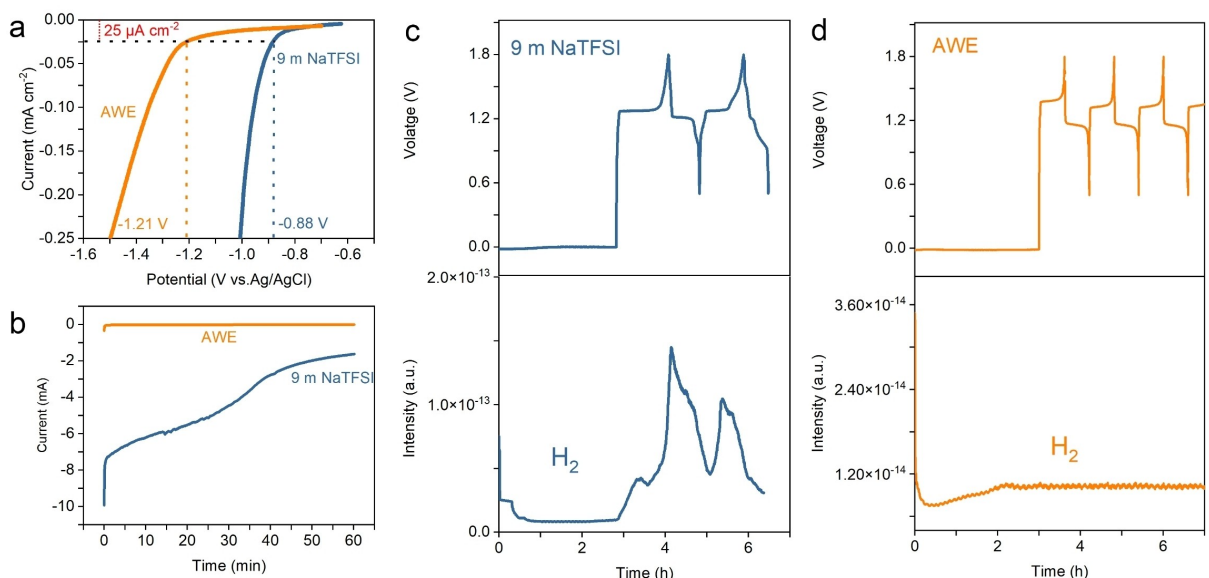


**Figure 2.** Cathodic stability of different electrolytes. a) LSV curves of AWE and 9 m NaTFSI electrolytes on Pt foil electrode measured in a three-electrode cell. Ag/AgCl and AC were used as the reference and counter electrodes, respectively. The dashed line at  $25 \mu\text{A cm}^{-2}$  represents the arbitrary defined onset value for electrolyte decomposition. b) Floating tests of AWE and 9 m NaTFSI electrolytes on Pt foil electrode at a fixed potential of  $-1.2 \text{ V}$  vs. Ag/AgCl. Online electrochemical mass spectrometry (OEMS) tests to quantitative determine the  $\text{H}_2$  evolution in NTP/NVP cells based on c) 9 m NaTFSI and d) AWE electrolyte at 1 C. The OEMS tests were performed in a voltage range of 0.5–1.8 V at a current density of 1 C.

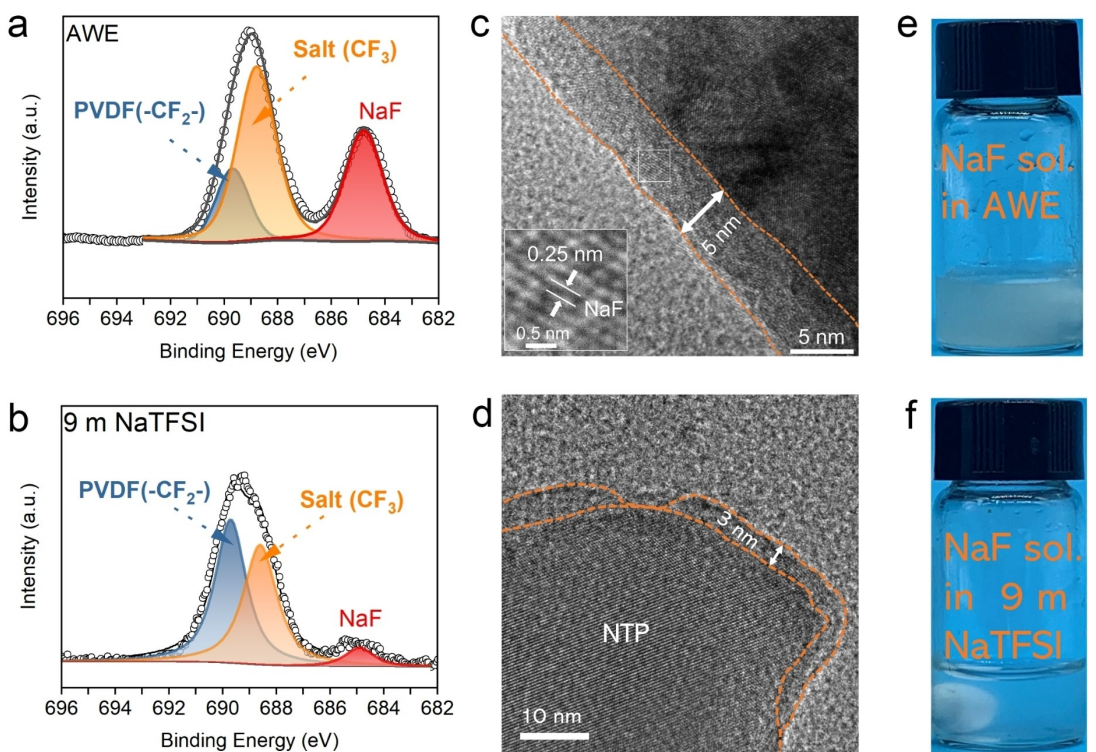


**Figure 3.** SEI on NTP anode generated in different electrolytes. XPS profiles of F1s spectra of NTP electrodes after 50 cycles in a) AWE and b) 9 m NaTFSI electrolytes. High-resolution TEM images of NTP after 50 cycles in c) AWE and d) 9 m NaTFSI electrolytes at 1 C. The different solubility of NaF powder in e) AWE and f) 9 m NaTFSI electrolyte.

layer is significantly lower when the 9 m NaTFSI is used as the electrolyte (Figure 3b), indicating more severe NaF dissolution in the 9 m NaTFSI compared with AWE electrolyte. To further confirm that a more robust NaF-rich SEI has been formed in

AWE, high resolution TEM images of NTP anode after cycling were collected as direct evidence. Figure 3(c) shows that a layer of partially crystalline species with a thickness of  $\sim 5 \text{ nm}$  fully covers the NTP surface uniformly. The interplanar space of this

layer was measured to be  $\sim 0.25$  nm, which agrees well with the d-spacing of NaF (200) plane (0.24 nm).<sup>[20]</sup> For comparison, the average thickness of covered SEI is  $\sim 3$  nm and part of NTP particle surface is even “naked” without NaF covering after cycling in 9 m NaTFSI, which suggested that the NaF-rich SEI formed in 9 m NaTFSI is not as robust as that formed in AWE (Figure 3d).

The critical role of the electrolyte in determining the robustness of SEI can be also reflected from the fact that the NTP/AC half-cell adopting SEI-protected NTP anode (from three-electrode cells in AWE electrolyte after 20 cycles) exhibits a low CE with poor cycle life in the presence of 9 m NaTFSI (Figure S9). In addition, the interphase between NTP electrode and AWE was analyzed using electrochemical impedance spectrum (EIS). After SEI formation formation in the first cycle, the interfacial resistance does not change significantly in subsequent cycles, revealing the robustness of the SEI layer (Figure S10) and its beneficial role in the improvement of the cycling performance of the NTP/AC half-cell. The more stable NaF-rich SEI on NTP surface in AWE can be also proved by direct comparing the solubility of NaF in 9 m NaTFSI and AWE. 5 mg NaF powder can be readily dissolved in 1.5 mL 9 m NaTFSI to obtain a clear colorless solution while the same amount of NaF cannot be fully dissolved in AWE (Figure 3e and

f), further confirming that the main inorganic components in SEI (NaF) are more robust in AWE than 9 m NaTFSI electrolyte. In short, the lack of free water molecules in AWE as discussed in the previous FTIR results in Figure 1(c) ensures sufficient stability of the NaF-rich SEI against electrolyte dissolution, which effectively inhibits HER kinetically.

Apart from the aforementioned parasite HER, constant dissolution of vanadium ions from Na-storage electrode materials such as NVP is another major challenge for aqueous SIBs. Given that the super-concentrated AWE lacks free water molecules, such mass dissolution issues of Na-storage electrodes are expected to be alleviated. It is well known that vanadium has a variety of oxidation states (+2, +3, +4, +5), which renders the concept of an all-vanadium redox-flow battery possible.<sup>[21]</sup> Since the redox couple of different dissolved vanadium species displays different reduction potential, CV tests could be used to gain insights into the dissolution behavior of vanadium species from NVP electrode. CV curves of NVP electrodes in Figure 4a show a pair of redox peaks located at 0.84 and 0.37 V (vs. Ag/AgCl) corresponding to reversible conversion of V(III)/V(IV) in NVP electrode.<sup>[22]</sup> Due to the loss of redox-active vanadium ions from the electrode, the intensity of this pair of peaks decreases remarkably in following cycles. Meanwhile, a new reduction peak gradually emerged and

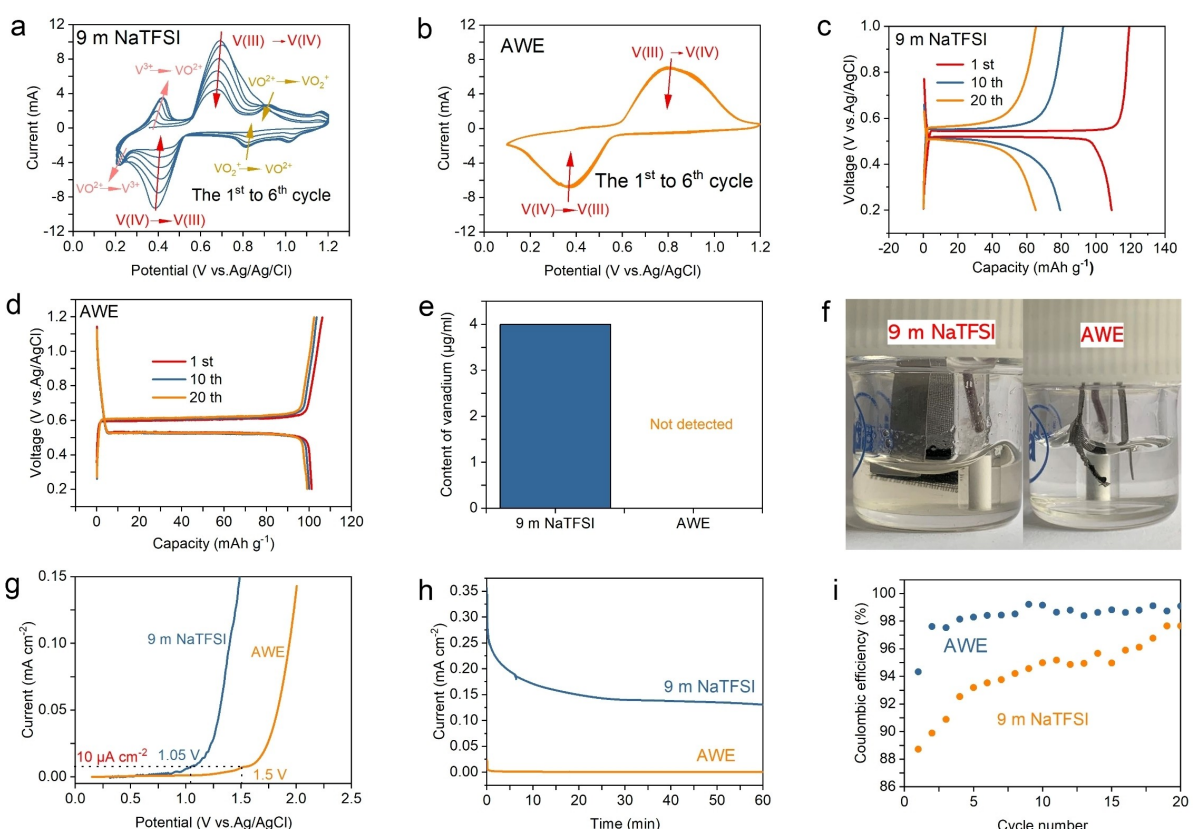


**Figure 4.** Vanadium dissolution from NVP electrodes in different electrolytes. CV profiles of NVP electrodes in a) 9 m NaTFSI and b) AWE electrolyte at a scan rate of 0.5 mVs<sup>-1</sup>. The charge-discharge curves of AC/NVP half-cell in c) 9 m NaTFSI and d) AWE electrolyte at 1 C. e) The dissolved amount of vanadium ions in different electrolytes after 50 cycles at 1 C and f) corresponding color changes. g) LSV curves of AWE and 9 m NaTFSI electrolytes on Pt foil electrode measured in a three-electrode cell. Ag/AgCl and AC were used as the reference and counter electrodes, respectively. h) Floating tests of AWE and 9 m NaTFSI electrolytes on Pt foil electrode at a fixed potential of 1.5 V vs. Ag/AgCl. i) Coulombic efficiency of AC/NVP half-cell in AWE and 9 m NaTFSI electrolytes.

increased at approximately 0.2 V vs. Ag/AgCl (converted to 0.397 V vs. NHE), which agrees well with the reduction potential of  $\text{VO}^{2+}/\text{V}^{3+}$  redox couple (~0.337 V vs. NHE).<sup>[23]</sup> In addition, another pair of peaks ascribed to  $\text{VO}^{2+}/\text{VO}^{2+}$  redox couple located at 0.8 V and 0.9 V vs. Ag/AgCl also evolved during CV tests, further revealing the constant dissolution of vanadium species from NVP electrode when 9 m NaTFSI is used as electrolyte.<sup>[24]</sup> In comparison, the peak of V(III)/V(IV) conversion in NVP electrode does not change noticeably in subsequent cycles when AWE is employed as the electrolyte and no new peaks associated with dissolved  $\text{V}^{3+}$  in electrolyte appeared (Figure 4b), indicating the beneficial effects of AWE in suppressing the vanadium dissolution from NVP. The suppressed vanadium dissolution from NVP in AWE can be also reflected in the charge-discharge profiles of AC/NVP half-cell (Figure 4c and d), as the cell supported by AWE electrolyte had a superior cycle stability while the cell based on the 9 m NaTFSI electrolyte displayed a rapid capacity decay in 20 cycles due to the loss of vanadium ions from NVP electrode. To better understand the vanadium dissolution from NVP electrode in AWE and 9 m NaTFSI, inductively coupled plasma optical emission spectroscopy-atomic emission spectroscopy (ICP-AES) analysis of content of dissolved vanadium ions after 20 cycles of AC/NVP cell were carried out. The content of dissolved vanadium ions in 9 m NaTFSI electrolyte amounts to  $3.9 \mu\text{g mL}^{-1}$  after cycling accompanied with the appearance of light yellow color, indicating severe vanadium dissolution (Figure 4e and f).<sup>[25]</sup> In contrast, the content of vanadium ion in AWE was below the detection limit of ICP-AES and the solution remained colorless after cycling, confirming the dramatically inhibited vanadium dissolution and extremely high electrochemical stability of NVP cathode in AWE.

Aside from reducing free water molecules to suppress the dissolution of SEI and vanadium-based electrodes, another beneficial role of the introduced ADN in AWE is the enhanced anodic stability due to the intrinsic high oxidative tolerance of ADN. Figure 4(g) shows that the anodic potential corresponding to a cut-off current of  $10 \mu\text{A cm}^{-2}$  was pushed to 1.5 V vs. Ag/AgCl in AWE. Floating tests of AWE electrolyte at 1.5 V vs. Ag/AgCl displays much lower anodic current compared with 9 m NaTFSI (Figure 4h), also confirming the higher oxidation stability of AWE. Consequently, an increase in average CE of AC/NVP half-cell can be observed when the AWE is adopted as the electrolyte (Figure 4i). Due to the enhanced oxidation stability, the AWE can even match the high-voltage Prussian blue cathode with 31% capacity loss after 250 cycles (Figures S11 and S12). As a result of both suppressed HER and elevated anodic stability in AWE, the ESWs can be eventually widened to 2.75 V on Pt working electrode, which is much larger than that of 9 m NaTFSI (1.95 V) under the identical testing conditions (Figure S13).

Electrochemical stability of electrolytes is known to be closely correlated with their solvation structures.<sup>[26]</sup> Therefore, spectroscopic characterizations and molecular dynamics (MD) simulations were used to probe the solvation structure of AWE electrolyte.  $^1\text{H}$  NMR shows that the  $^1\text{H}$  chemical shift of pure  $\text{H}_2\text{O}$  at 4.26 ppm decreases to 3.87 ppm in 9 m NaTFSI electrolyte (Figure 5a), in accordance with the shielding effect of salt on water which leads to the strengthening of O-H covalent bonding and reduced activity of water.<sup>[27]</sup> Compared with pure ADN solvent where the  $^1\text{H}$  chemical shift locates at 2.46 and 1.72 ppm (Figure S14), the  $^1\text{H}$  signal of ADN in AWE shifted upfield to 2.17 and 1.43 ppm respectively, revealing the strong interaction between ADN and  $\text{Na}^+$ . Moreover, we note that the

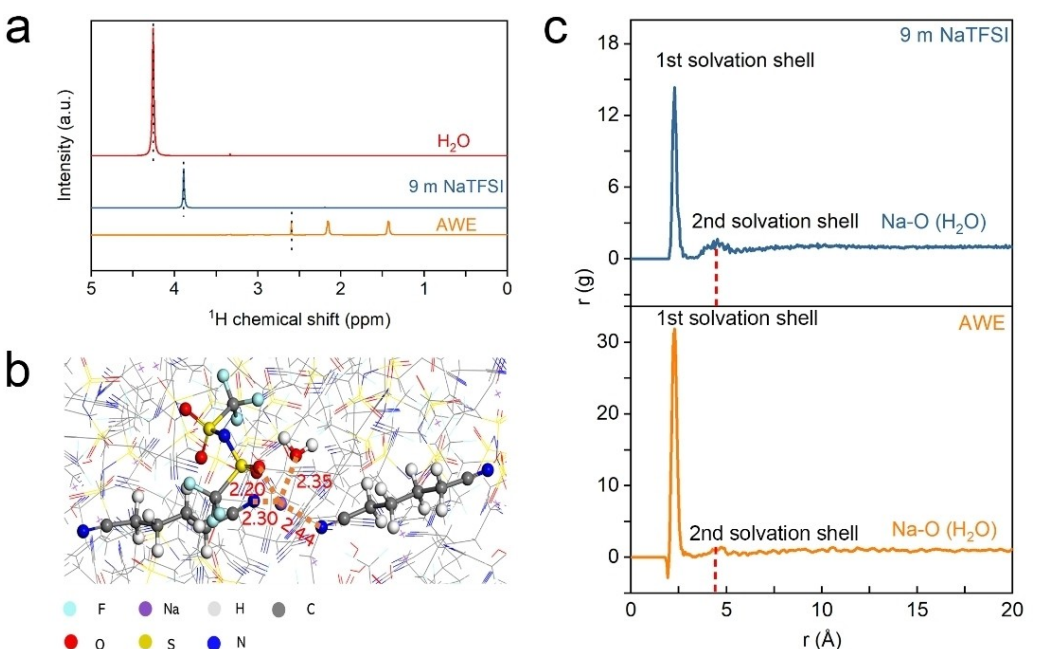


**Figure 5.** Solvation structures of different electrolytes. a) Chemical shifts for  $^1\text{H}$  nuclei in AWE and 9 m NaTFSI with pure water as a comparison. b) Solvation structure of the AWE electrolyte obtained from MD simulation. c) RDF plots of  $\text{Na}^+-\text{O}(\text{H}_2\text{O})$  in the 9 m NaTFSI and AWE electrolytes.

upfield shift of  $^1\text{H}$  chemical shift of water in AWE (2.60 ppm) is much more prominent compared with that of 9 m NaTFSI (3.87 ppm), indicating that the introduced ADN could reduce the activity of water to a greater degree.<sup>[28]</sup> Next, the solution structure of AWE is further studied by MD simulations. Figure 5(b) shows that on average one TFSI $^-$  anion, one water molecule and two ADN molecules are observed in each Na $^+$  primary solvation shell in AWE electrolyte. Since the molar ratio of Na $^+$  to H $_2\text{O}$  in AWE is exactly 1:1, this suggests that almost all water molecules are confined in the solvation sheath of Na $^+$  and the excess Na $^+$  ions are coordinated by ADN, which can be also supported by Raman results (Figure S15). Radial distribution functions (RDF) analysis can provide more detailed information about the solvation environment of water molecule in the AWE electrolyte. According to the RDF plots in Figure 5(c), almost all water molecules participate in the first solvation shell (also called primary solvation shell) of Na $^+$  in AWE electrolyte, consistent with previous FTIR results in Figure 1(c). Meanwhile, a small portion of water molecules can be observed in the second solvation shell of Na $^+$  in 9 m NaTFSI electrolyte, indicating that some water molecules with higher activity exist. Since the water molecule with a high activity (including free water molecules) plays a decisive role in dissolving protective SEI and vanadium ions as well as participating in OER, confining all water molecules within the first solvation shell of Na $^+$  with decreased activity would alleviate the HER, suppress vanadium ion dissolution, and inhibit OER, all of which are favorable for the long-cycle life of aqueous SIBs.

Finally, the electrochemical performance of NVP/NTP full cell with AWE electrolyte was evaluated in a voltage range of 0.5–1.8 V as displayed in Figure 6(a). It delivers an initial discharge capacity of  $\sim 96 \text{ mAh g}^{-1}$  with very small voltage polarization at 1 C. Impressively, the full cell with AWE electrolyte retains  $\sim 90\%$  of initial capacity after 100 cycles at 1 C with an average CE of 99.5%. For comparison, the capacity decreases to less than  $50 \text{ mAh g}^{-1}$  in merely 60 cycles with much lower CE in the presence of 9 m NaTFSI electrolyte. In addition, large fluctuation of discharge capacity can be observed using 9 m NaTFSI electrolyte, which is likely caused by the abrupt escaping of evolved H $_2$  bubble from the NTP surface (Figure 6b). At a higher rate of 5 C, the long-term stability of the full cell using AWE is even more superior and 71% capacity retention can be achieved with an average CE of 96.6% after 1000 cycles (Figure 6c), which is much better than the cell based on 9 m NaTFSI electrolyte (20% capacity retention). As a side note, the full cell based on AWE also displays limited self-discharge behavior due to the suppressed parasite HER (Figure S16).

## Conclusion

In summary, ADN was chosen as the co-solvent to obtain a super-concentrated aqueous sodium electrolyte (Na $^+/\text{H}_2\text{O}=1$ , molar ratio) where almost all water molecules are confined within the primary solvation shell of Na $^+$ . Such a unique solvation structure lacking free water molecules not only enables the formation of a robust NaF-rich SEI suppressing HER

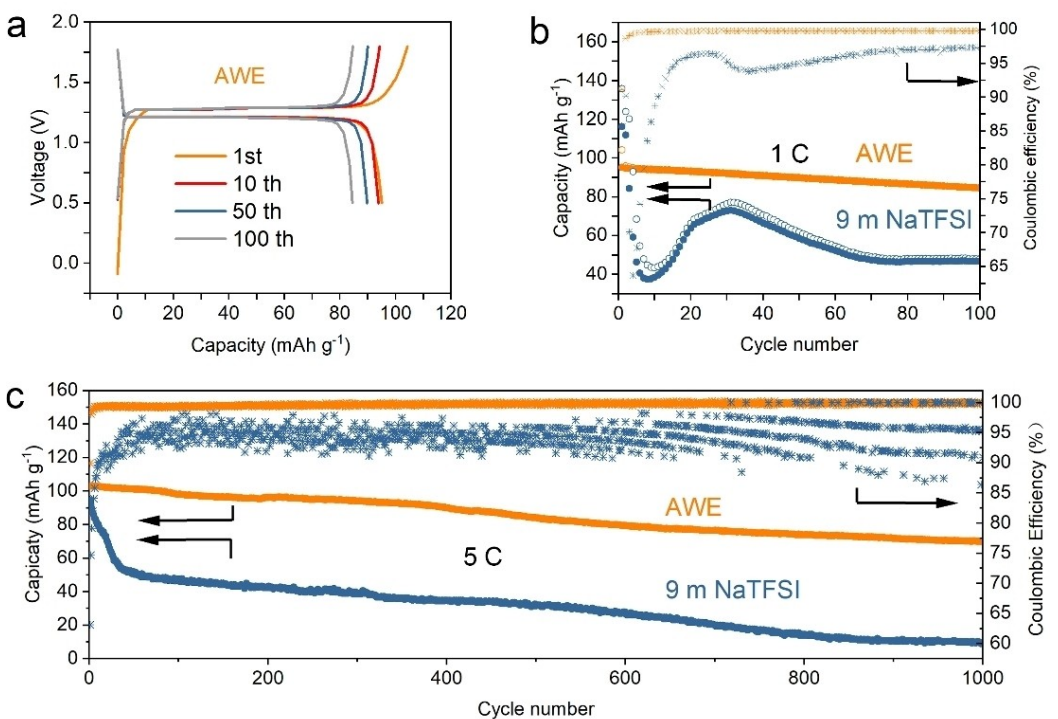


**Figure 6.** Electrochemical performance of NVP/NTP full cells based on different electrolytes. a) The 1st, 10th, 50th and 100th charge-discharge curves of the NVP/NTP full cell at 1 C in AWE electrolyte. b) Cycling performance of NVP/NTP full cell at 1 C. c) Long term cycling performance of NVP/NTP full cell at 5 C.

effectively, but also alleviates mass dissolution of vanadium-based electrodes. Moreover, due to the intrinsic high anodic stability of ADN, the oxidative decomposition potential of the electrolyte was also elevated, which eventually widens the ESW to 2.75 V. Paired with this electrolyte, the  $\text{Na}_3\text{V}_2(\text{PO}_4)_3/\text{NaTi}_2(\text{PO}_4)_3$  full battery achieves an average CE of 99.6% with 71% capacity retention for 1000 cycles. In addition, the hybrid aqueous electrolyte possesses a low freezing point of  $-79^\circ\text{C}$  with superior low-temperature conductivity due to the disrupted hydrogen bond among water molecules and also the eutectic nature, which makes it even more appealing in wide-temperature applications.

## Acknowledgements

This work was financially supported by National Natural Science Foundation of China (21975271), Shandong Natural Science Foundation (Grant No. ZR2020ZD07, ZR2021QB106). J. W. Zhao particularly acknowledges the financial support from the Youth Innovation Promotion Association of CAS (2019214) and Shandong Energy Institute (Grant No. SEI I202127).

## Conflict of Interest

The authors declare no conflict of interest.

## Data Availability Statement

The data that support the findings of this study are available from the corresponding author upon reasonable request.

**Keywords:** cycle life · hybrid electrolyte · sodium-ion battery · solvation structure · vanadium dissolution

- [1] M. Armand, J. M. Tarascon, *Nature* **2008**, *451*, 652–657.
- [2] a) Z. Yang, J. Zhang, M. C. W. Kintner-Meyer, X. Lu, D. Choi, J. P. Lemmon, J. Liu, *Chem. Rev.* **2011**, *111*, 3577–3613; b) N. Choi, Z. Chen, S. A. Freunberger, X. Ji, Y.-K. Sun, K. Amine, G. Yushin, L. F. Nazar, J. Cho, P. G. Bruce, *Angew. Chem. Int. Ed.* **2012**, *51*, 9994–10024; *Angew. Chem.* **2012**, *124*, 10134–10166; c) H. Kim, H. Kim, Z. Ding, M. H. Lee, K. Lim, G. Yoon, K. Kang, *Adv. Energy Mater.* **2016**, *6*, 1600943; d) P. Barpanda, G. Oyama, S. Nishimura, S. Chung, A. Yamada, *Nat. Commun.* **2014**, *5*, 4358.
- [3] W. Li, J. R. Dahn, D. S. Wainwright, *Science* **1994**, *264*, 1115–1118.
- [4] a) W. Song, X. Ji, Y. Zhu, H. Zhu, F. Li, J. Chen, F. Lu, Y. Yao, C. E. Banks, *ChemElectroChem* **2014**, *1*, 871–876; b) L. Zhang, T. Huang, A. Yu, J.

- Alloys Compd.* **2015**, *646*, 522–527; c) Q. Zhang, C. Liao, T. Zhai, H. Li, *Electrochim. Acta* **2016**, *196*, 470–478.
- [5] a) L. Suo, O. Borodin, T. Gao, M. Olgui, J. Ho, X. Fan, C. Luo, C. Wang, K. Xu, *Science* **2015**, *350*, 938–943; b) L. Suo, O. Borodin, Y. Wang, X. Rong, W. Sun, X. Fan, S. Xu, M. A. Schroeder, A. V. Cresce, F. Wang, C. Yang, Y. Hu, K. Xu, C. Wang, *Adv. Energy Mater.* **2017**, *7*, 1701189.
- [6] S. Chen, J. Ishii, S. Horiuchi, M. Yoshizawa-Fujita, E. I. Izgorodina, *Phys. Chem. Chem. Phys.* **2017**, *19*, 17366–17372.
- [7] Y. Sui, M. Yu, Y. Xu, X. Ji, *J. Electrochem. Soc.* **2022**, *169*, 030537.
- [8] a) F. Wang, O. Borodin, M. S. Ding, M. Gobet, J. Vatamanu, X. Fan, T. Gao, N. Eidson, Y. Liang, W. Sun, S. Greenbaum, K. Xu, C. Wang, *Joule* **2018**, *2*, 927–937; b) J. Chen, J. Vatamanu, L. Xing, O. Borodin, H. Chen, X. Guan, X. Liu, K. Xu, W. Li, *Adv. Energy Mater.* **2020**, *10*, 1902654.
- [9] J. Liu, C. Yang, X. Chi, B. Wen, W. Wang, Y. Liu, *Adv. Funct. Mater.* **2022**, *32*, 2106811.
- [10] H. Zhang, B. Qin, J. Han, S. Passerini, *ACS Energy Lett.* **2018**, *3*, 1769–1770.
- [11] a) S. Li, D. Zhao, P. Wang, X. Cui, F. Tang, *Electrochim. Acta* **2016**, *222*, 668–677; b) D. Farhat, J. Maibach, H. Eriksson, K. Edström, D. Lemordant, F. Ghamous, *Electrochim. Acta* **2018**, *281*, 299–311.
- [12] a) Y. Marcus, *J. Solution Chem.* **1984**, *13*, 599–624; b) V. Gutmann, *Electrochim. Acta* **1976**, *21*, 661–670; c) H. Duncan, N. Salem, Y. Lebdeh, *J. Electrochem. Soc.* **2013**, *160*, A838–A848.
- [13] P. A. Robertson, I. A. Lobo, D. J. D. Wilson, E. G. Robertson, *Chem. Phys. Lett.* **2016**, *660*, 221–227.
- [14] W. J. Geary, *Coord. Chem. Rev.* **1971**, *7*, 81–122.
- [15] W. Yang, X. Du, J. Zhao, Z. Chen, J. Li, J. Xie, Y. Zhang, Z. Cui, Q. Kong, Z. Zhao, C. Wang, Q. Zhang, G. Cui, *Joule* **2020**, *4*, 1557–1574.
- [16] Q. Nian, J. Wang, S. Liu, T. Sun, S. Zheng, Y. Zhang, Z. Tao, J. Chen, *Angew. Chem. Int. Ed.* **2019**, *58*, 16994–16999; *Angew. Chem.* **2019**, *131*, 17150–17155.
- [17] R. Kühnel, D. Reber, C. Battaglia, *ACS Energy Lett.* **2017**, *2*, 2005–2006.
- [18] a) J. Zhang, J. Gai, K. Song, W. Chen, *Cell Rep. Phys. Sci.* **2022**, *3*, 100868; b) T. Li, X. Zhang, P. Shi, Q. Zhang, *Joule* **2019**, *3*, 2647–2661.
- [19] T. Jin, X. Ji, P. Wang, K. Zhu, J. Zhang, L. Cao, L. Chen, C. Cui, T. Deng, S. Liu, N. Piao, Y. Liu, C. Shen, K. Xie, L. Jiao, C. Wang, *Angew. Chem. Int. Ed.* **2021**, *60*, 11943–11948.
- [20] B. Han, Y. Zou, Z. Zhang, X. Yang, X. Shi, H. Meng, H. Wang, K. Xu, Y. Deng, M. Gu, *Nat. Commun.* **2021**, *12*, 3066.
- [21] W. Lu, X. Li, H. Zhang, *Phys. Chem. Chem. Phys.* **2018**, *20*, 23–35.
- [22] S. Chen, C. Wu, L. Shen, C. Zhu, Y. Huang, K. Xi, J. Maier, Y. Yu, *Adv. Mater.* **2017**, *29*, 1700431.
- [23] X. Li, H. Zhang, Z. Mai, H. Zhang, I. Vankelecom, *Energy Environ. Sci.* **2011**, *4*, 1147–1160.
- [24] J. Yue, L. Lin, L. Jiang, Q. Zhang, Y. Tong, L. Suo, Y. Hu, H. Li, X. Huang, L. Chen, *Adv. Energy Mater.* **2020**, *10*, 2000665.
- [25] S. Liu, J. He, D. Liu, M. Ye, Y. Zhang, Y. Qin, C. C. Li, *Energy Storage Mater.* **2022**, *49*, 93–101.
- [26] J. Xu, X. Ji, J. Zhang, C. Yang, P. Wang, S. Liu, K. Ludwig, F. Chen, P. Kofinas, C. Wang, *Nat. Energy* **2022**, *7*, 186–193.
- [27] a) M. H. Lee, S. J. Kim, D. Chang, J. Kim, S. Moon, K. Oh, K. Park, W. M. Seong, H. Park, G. Kwon, B. Lee, K. Kang, *Mater. Today* **2019**, *29*, 26–36; b) P. Gilli, G. Gilli, *J. Mol. Struct.* **2010**, 972, 2–10.
- [28] J. Xie, Z. Liang, Y. Lu, *Nat. Mater.* **2020**, *19*, 1006–1011.

Manuscript received: June 2, 2022  
Revised manuscript received: July 5, 2022  
Version of record online: August 3, 2022